

Friction and adhesion of different structural defects of graphene

Manoj Tripathi^a, Firas Awaja^b, Rafael A. Bizão^{c,a}, Stefano Signetti^d, Erica Iacob^e, Guido Paolicelli^f, Sergio Valeri^{f,g}, Alan Dalton^a, Nicola [Maria](#) Pugno^{a,h,i,*}

^a *Department of Mathematics and Physical sciences, University of Sussex, Brighton, BN1 9RH, UK*

^b *Department of Orthopaedic Surgery, Medical University Innsbruck, Innrain 36, Innsbruck, Austria*

^c *Applied Physics Department, State University of Campinas, Campinas-SP, 13083-959, Brazil*

^d *Department of Mechanical Engineering, Korea Advanced institute of Science and Technology (KAIST), 291 Daehak-ro, Yuseong-gu, Daejeon 34141, Republic of Korea*

^e *Centre for Materials and Microsystems, Fondazione Bruno Kessler, via Sommarive 18, I-38123 Trento, Italy*

^f *Istituto Nanoscienze, Consiglio Nazionale delle Ricerche, via G. Campi 213/a, 41125- Modena, Italy*

^g *Dipartimento di Scienze Fisiche Informatiche e Matematiche (FIM), Università di Modena e Reggio Emilia, Via Campi 213/a, I-41125 Modena, Italy*

^h *School of Engineering and Materials Science, Queen Mary University of London, Mile End Road, E1 4NS London - United Kingdom*

ⁱ *Ket Lab, Edoardo Amaldi Foundation, Italian Space Agency, Via del Politecnico snc, I-00133 Roma, Italy*

* Corresponding author: nicola.pugno@unitn.it

Keywords: AFM, Graphene, Defects, Friction, Adhesion

Abstract: Graphene structural defects, namely edges, step-edges and wrinkles are susceptible to severe mechanical deformation and stresses under frictional operations. Applied forces cause deformation by folding, buckling, bending and tearing the defective sites of graphene, which lead to a remarkable decline in normal load and friction bearing capacity. In this work, we experimentally quantified the maximal normal and friction forces corresponding to the damage thresholds of the different investigated defects as well as their pull-out (adhesion) forces. Horizontal wrinkles (with respect to the basal plane, i.e. folded) sustained the highest normal load, up to 317 nN, during sliding, whereas for vertical (i.e. standing collapsed) wrinkles, step-edges and edges, the load bearing capacities are up to 113 nN, 74 nN and 63±5 nN, respectively. The related deformation mechanisms were also experimentally investigated by varying the normal load up to the initiation of the damage from the investigated defects and extended with the numerical results from Molecular Dynamics and Finite Element Method simulations.

Introduction

Graphene is a robust choice for coating surfaces to achieve improved tribological properties such as superlubricity ¹, tuned friction ², and high load bearing capability which results in antiwear characteristics ³. Graphene failure under frictional loads ⁴⁻⁷ becomes predominant in the presence of structural defects that are thus taking a central interest in the materials research community due to their

implication on the advanced applications of graphene related materials. Most of the reported exotic characteristics of graphene are refer to defect-free films thus neglecting the dramatic role of structural flaws and imperfections. Failure of graphene mostly occurs at structural defects such as the edges (*E*, i.e. the perimeter of an atomic layer over a different substrate), step-edges (*SE*, i.e. the perimeter of an atomic layer over another atomic layer), wrinkles (*Wr*)⁸⁻⁹, grain boundaries (*GB*)¹⁰⁻¹¹ and vacancies¹². These defects introduce significant alterations in the graphene properties that often compromise its durability and functionality. Grain boundaries and wrinkles, for example, can severely weaken the mechanical strength of graphene membranes. Indeed, the fracture strength might be decreased by order of magnitude^{10, 13}. Isolated defects, such as mono-vacancies and Stone-Wales dislocations, slits, and holes also compromise the mechanical properties of graphene^{12, 14-16}.

E and *SE* are potentially the most dire defects among lamellar materials. Several reports explained that atoms belonging to *E/SE* behave differently from the atoms of basal plane in both physical^{14,17-18} and chemical aspects^{11, 19} due to the presence of dangling bonds. Atomic Force Microscopy (AFM) studies revealed that the mechanical response of the *E/SE* defects is also strongly influenced by the size and shape of the AFM tip, environmental conditions (such as the presence of airborne impurities, nitrogen atmosphere and vacuum), and surface energy landscape, as reported extensively²⁰⁻²⁵. For example, large energy barriers, i.e. the difference between maximum potential energy of slide probe at basal plane and at step-edge, was proposed by Ye and Martini²⁶ as the primary cause of graphene rupture during AFM operations. Other structural defects include *Wr* and *GB*, which are commonly produced during chemical vapour deposition (CVD) of polycrystalline graphene^{9, 27}. These structural defects have higher binding energy than basal graphene plane which is responsible for higher interaction with foreign particles and higher friction forces²⁷. Yu *et al.*²⁷ revealed enhanced sp³ state and lower van der Waals stabilization of *Wr* as compared to graphene basal plane, which causes the *Wr* detachment from the substrate. Vasic *et al.*¹⁹ found that the bearing loading capacity of graphene (i.e threshold of normal force to initiate wear) significantly drops (by nearly 1 order of magnitude) in the presence of wrinkles.

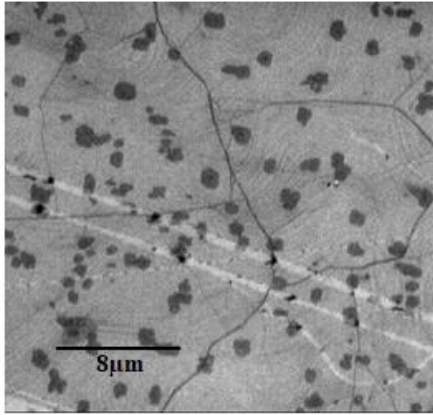
AFM is one of the most effective techniques to study nano-structural surfaces and defects²⁸⁻²⁹. In particular, its sensitivity is able to detect short-range interactions at the atomic level³⁰ and to manipulate structures at the nano³¹ and atomic scale³². Friction Force Microscopy (FFM), a subcategory of AFM technique, allows for the detection of friction forces from atomic to micro scale. Sliding of the tip along the fast scan axis in contact with the substrate generates a lateral force (F_L) on the apex which causes the cantilever torsion around its longitudinal direction; accordingly, graphene surface defects, like vacancies, adsorbed atoms and molecules produces a visible contrast in the lateral force image²². Higher friction forces at *E/SE* and *Wr* are attributed to the Schwoebel-Ehrlich barrier at atomic steps^{23, 33} and to the *ratchet effect*³⁴⁻³⁵ respectively. Recently, friction and wear phenomena of the edge of graphene on silica substrate have been explained through buckling and lower interaction of the edge atoms with silica surface¹⁹ whereas the height of the *E* region was reported as higher than that of graphene basal plane²⁰ (due to *puckering* effect) and is responsible for the folding and tearing of graphene edges.

In the present work, we compared the load bearing capacity, friction and adhesion forces for different types of line defects of 2D material, namely *E*, *SE* and *Wr* (horizontal and vertical types). In particular, we elucidated the frictional stability of structural defects for polycrystalline graphene. We also endeavored to comprehensively investigate the mechanical deformation phenomena of the *E*, *SE* and *Wr* of the graphene layer, conducted through the systematic increase of the applied normal force (F_N) and measuring the friction forces (F_F). Molecular Dynamics (MD) simulations have been conducted in order to explicate the experimental observations.

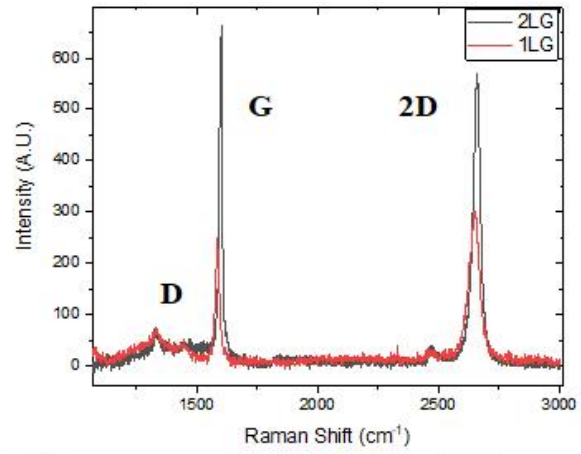
Results and Discussion

Commercially obtained CVD produced graphene transferred on silica substrate have been used in our investigation. The scanning electron microscopy (SEM) image illustrating the distribution of single graphene layer (*1LG*, bright color), bi-layer (*2LG*, dark patches) and *Wr* in fig.1a. The presence of *1LG* and *2LG* are also verified by Raman spectroscopy by measuring the ratio intensity of 2D and G peak ³⁶, fig. 1b. The AFM topography of graphene is showing various landscape namely *1LG*, *2LG*, *SE* and *Wr* in fig. 1c. The high-resolution 3D-AFM topography shows a morphological contrast among the *Wr* and graphene basal plain of *1LG* and *2LG* in fig. 1d. The distribution of the *Wr* and the intrinsic ripples in the graphene significantly influence its roughness and topological conformation. The roughness (root mean square) of *1LG* is measured as 0.320 nm is slightly higher than *2LG*, which is 0.314 nm. The roughness of transferred CVD graphene is associated to the method of transfer, graphene thickness, substrate interaction and tip radius used for the investigation³⁷. In the present work, silicon cantilever tip (apex radii ~ 25 nm) is used for the roughness measurement and for the low load friction measurement (see supplementary information [figure_S1](#) for a collection of images at different locations). Subsequently, diamond-like carbon (DLC) coated tip has been used for high load measurements to avoid any wear at the tip apex (radii ~ 100 nm).

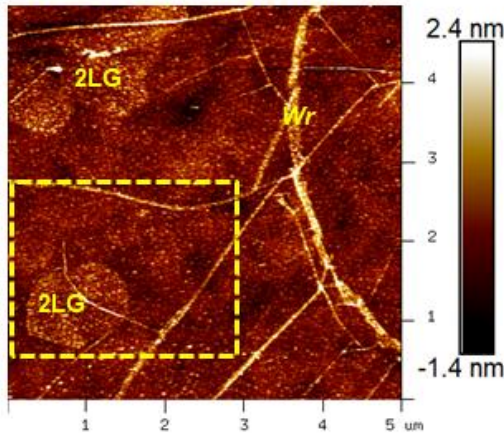
a SEM image of CVD graphene



b Raman spectra of CVD graphene



c AFM topography Gr/Si_CVD



d

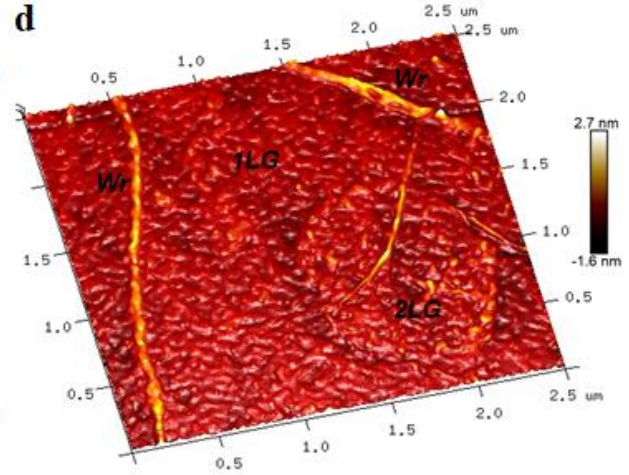


Figure 1: Topographical information of CVD graphene on silica substrate. (a) SEM image of the CVD graphene showing distribution of *Wr* and 2LG (dark patches). (b) Raman spectra confirming the presence of 2LG and 1LG (from ratio of 2D and G) with structural disorder (D-peak). (c) AFM topographical image showing the basal plane consisting of 1LG, some 2LG islands and the crossed network of *Wr*. (d) High resolution 3-D AFM topography showing morphological contrast between *Wr* and graphene basal plain.

Wr in the graphene sheet show a significant contrast in the friction map, fig. 2a, which is quantitatively revealed by combining topographical and lateral force profile, fig. 2b. The trace and re-trace scanning direction of the tip is showing highest lateral force at the *Wr* and lowest value at the 2LG with intermediate values of 1LG and SE. The area under the lateral force loop is associated with friction dissipation by the cantilever during sliding, which is highest at the *Wr* region. The frictional characteristics of the *Wr* depends on several factors: altitude, width, orientation to the fast scan axis and the normal force (F_N) applied. The analysis proposed on fig. 2(c, d) at constant load $F_N \approx 35$ nN compare different *Wr* orientation in the same image i.e. measured with same tip condition. We obtained maximum value of the F_F for *Wr* axis of fixed amplitude of 2 nm oriented at 90° to the scanning axis and minimal value for *Wr* oriented

nearly 7° with respect to the scan axis showing the tendency towards parallel alignment of the Wr axis leads to least friction force.

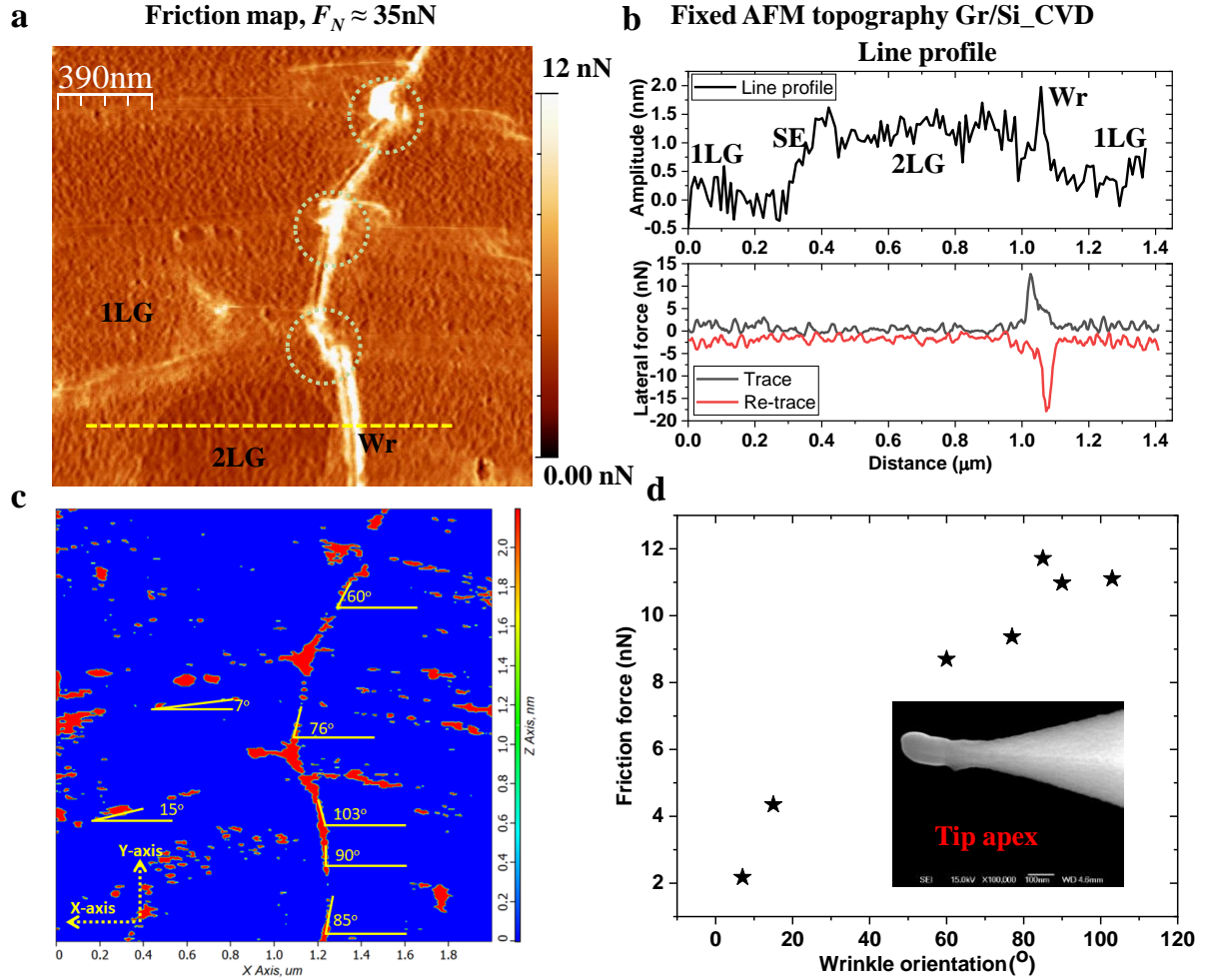


Figure 2: Friction force as a function of Wr orientation. (a) Friction map that include lateral force values measured in trace and re-trace scanning direction of cantilever on CVD graphene. It is showing highest F_F on Wr , lowest on 2LG (bright color corresponds to higher friction force) and intermediate for 1LG. (b) Topography and lateral force line profile along 2LG region and a Wr (yellow dashed line on panel a). (c) Filtered topography image, Wr have been highlighted making red regions with amplitude of 2 nm. Their orientation is measured with respect to x-axis corresponding to fast scan direction. (d) Friction force as a function of Wr orientation at $F_N = 35\text{ nN}$. Inset is showing SEM image of the tip used for the friction measurement.

The orientation of the Wr has a significant impact on their friction and load bearing capabilities in sliding operations. Two examples are illustrated in fig. 3 and fig. 4, in which Wr axis is oriented to the scan axis of $\sim 64^\circ$ and $\sim 90^\circ$ respectively. Under applied F_N range from -50 nN to 320 nN, Wr oriented at $\sim 64^\circ$ (fig.3c) can bear a higher $F_N \approx 260\text{ nN}$ than at Wr axis oriented $\sim 90^\circ$ at the critical $F_N \approx 113\text{ nN}$ (fig.4 d,

h). It is suggesting that the critical load scale as the component of F_F perpendicular to the Wr , which we may refer to as the *cutting force*.

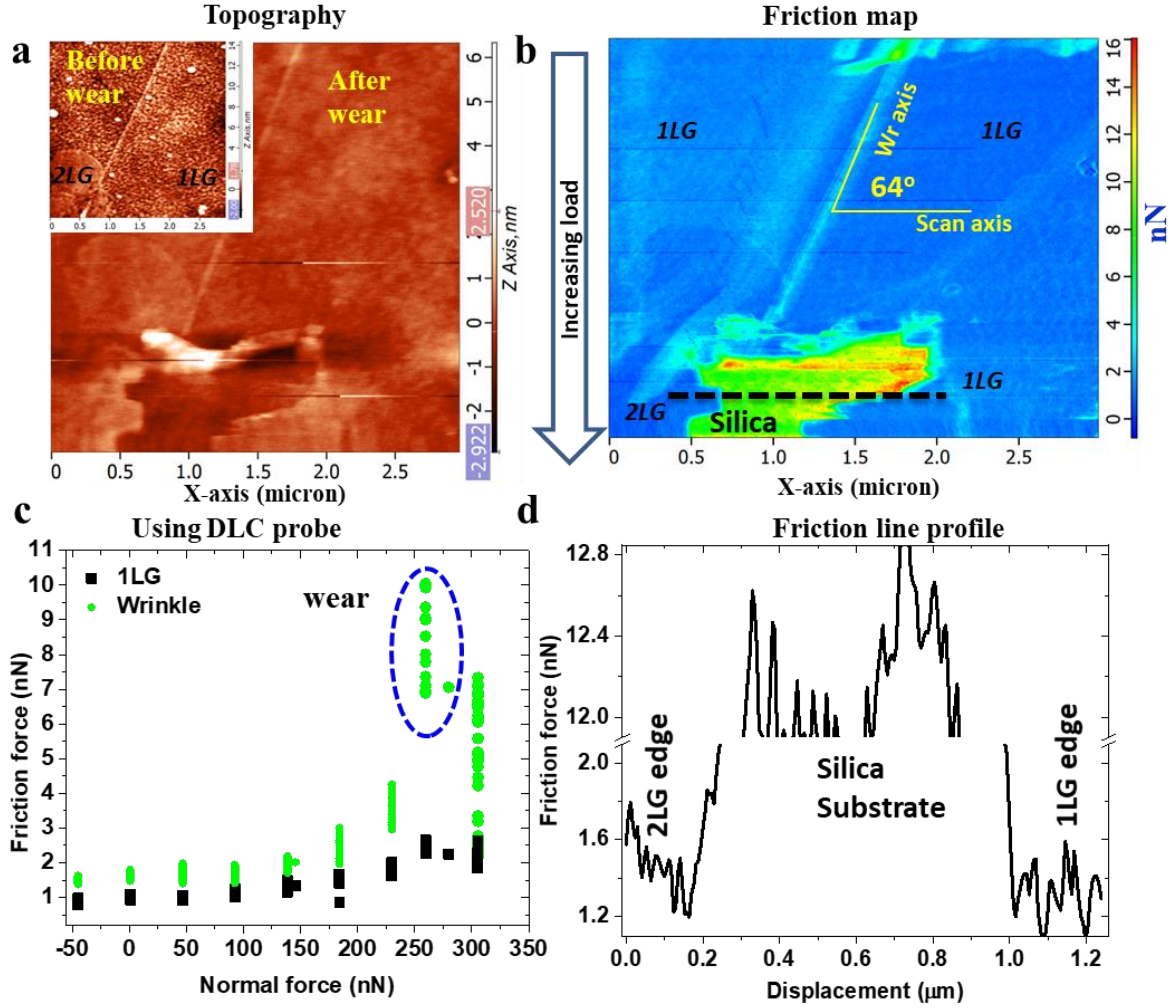


Figure 3: Surface wear of Wr and $1LG$ measured with DLC probes. (a) AFM topography of the CVD graphene before (inset) and after wear. (b) Friction map of the same region showing distribution of F_F along the Wr and $1LG$. The F_N is increased at the interval of 60 seconds from top to bottom direction (slow scan axis) up to wear of the Wr region. The orientation of the Wr is nearly 64° with respect to the fast scan axis of the cantilever. (c) F_F as a function of F_N in the $1LG$ region and at the Wr up to wear of the Wr at $F_N = 260$ nN as marked by a sudden increase of F_F (dashed ellipse). Defect free $1LG$ is showing lower F_F than the Wr for all F_N values and no wear has been observed up to 300 nN. (d) Friction profile.

The Wr axis oriented $\sim 90^\circ$ with respect to the cantilever scan direction, is ideal to study the phenomenon of friction induced deformation, since it induces maximum deflection in the Wr . The topography and F_L maps are reported in fig. 4 for increasing F_N equal to -100 nN (fig. 4 (a,e), 11 nN (b, f), 68 nN (c, g), and 113 nN (d, h) shows different extent of deflection up to wear for the highest normal load. At lower values of F_N (around -100 nN, where adhesion is prevailing), the wrinkle is more resistant to bending and into

traction and shows broader F_F distribution along its length fig. 4(a, e). With the increase of $F_N \approx 11$ nN, a lateral elastic deflection occurs towards the scanning direction of the tip (fig. 4 (b, f)). At $F_N \approx 68$ nN several local folds, observed at 11 nN, merge into a larger global deflection, overcoming the stiffness and the adhesion on the substrate of the whole wrinkle in fig. 4 (c, g). At $F_N \approx 113$ nN (fig. 4(d, h)), initiation of the wear has been observed along the Wr axis, leading to significant increase of the F_F values as marked by black arrow. The schematic view illustrates the respective deflections of the Wr at different F_N and the wear initiated region. Nanoscale frictional characteristics of $1LG$ is associated to the several factors like substrate roughness³⁷, electron-phonon coupling³⁸ and the puckering effect, in which graphene elastically buckled out in front of the sliding tip²⁰. The presence of the Wr enhances the F_F due to its bending flexibility during the scanning of the cantilever as compare to the defect free $1LG$ for all applied F_N . We did not observe any wear in the defect free basal of $1LG$ in the applied load range.

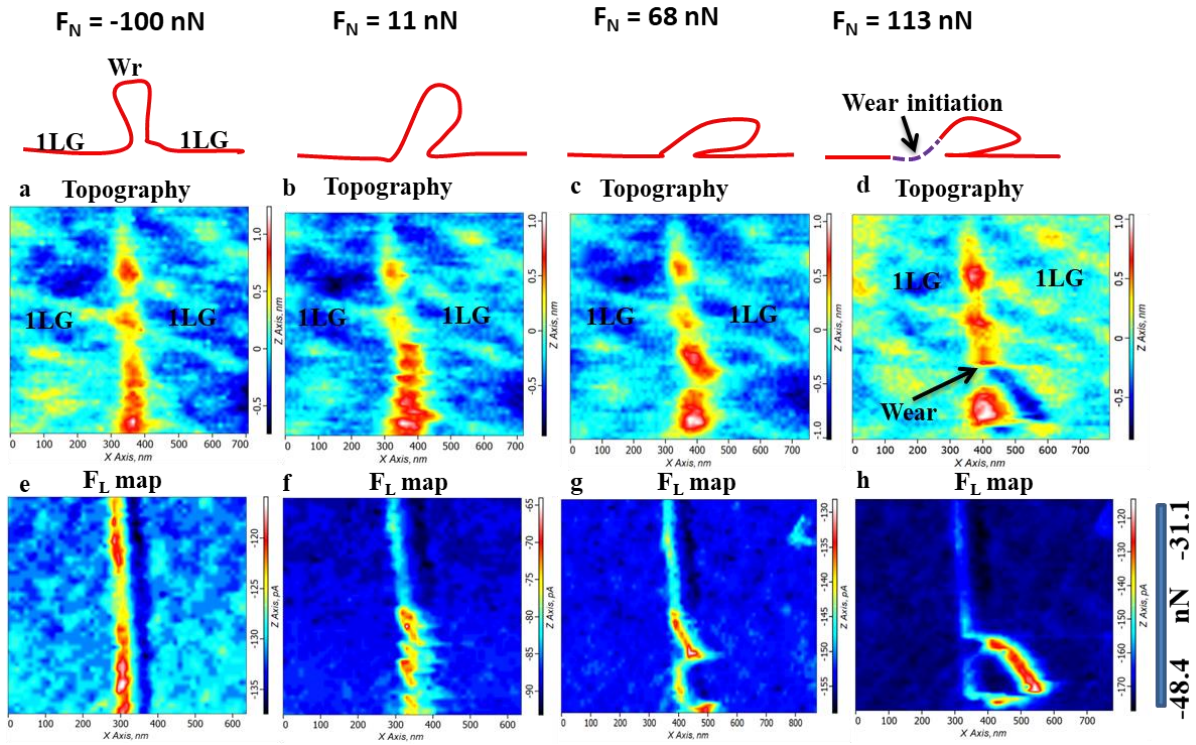


Figure 4: Deformation and wear of the vertical Wr in CVD graphene. Topography (a-d) and F_L map (with scanning direction from left to right) (e-h) at increasing normal force, from -100 nN to 113 nN. The orientation of the wrinkle is nearly 90° to the fast scanning direction. The height of the wrinkle around 1 nm, changes at different F_N , indicating normal and lateral deformations. The negative value of the F_L map is due to the use of single channel “trace”. The “wear” has been observed only at the highest normal load of 113 nN.

The worn region of graphene appears to be the weakest attributes for further damage and rupturing due to the generation of the edges. The height of the edges relates to the friction signal in which thicker edges of 2LG has slightly higher friction than the 1LG edge as illustrated by friction line profile in fig 3(b, d) and [figure S2](#) (a-d) for both CVD and mechanical exfoliated graphene respectively. Nevertheless, the frictional characteristic of the graphene *E* is different from the *Wr*. The latter showed bending and stretching; while *E* and *SE* display the folding and buckling mechanisms before wear that will be discussed in the present section. Here, we compare the F_F values for *E*, *Wr* and defect free 1LG graphene in a single acquisition for different F_N values. Fig. 5 shows topographies (a-d) and F_F maps (e-h) of *Wr*s (horizontal and vertical configurations), *E*, 1LG and silica substrate under F_N (namely, 11 nN, 68 nN, 113 nN and 205 nN). Initially, the wear of the graphene is observed in the *E* region at around 68 nN, for vertical wrinkle at 113 nN (marked by a dashed circle) whereas the horizontal *Wr* was unaffected even at the highest F_N of ~320 nN, thus more robust against “cutting”. The increment of F_N after 11 nN further removed the graphene carbon atoms from the *E* region via folding and tearing as the “peel induced rupture” mechanism³⁹. F_F vs F_N values are reported in fig. 5i, j, showing highest F_F for the silica substrate and lowest for the CVD 1LG with intermediate trends of *Wr* and *E*. This clearly shows the role of single layer graphene in reducing friction as solid-state lubricant, despite the possible presence of defects. In fig. 5j the two different *Wr* topologies are compared in terms of F_F . Vertical *Wr* shows comparable F_F to the horizontal configuration for different F_N up to 200 nN of F_N . Nevertheless, horizontal *Wr* is showing lower F_F at high load conditions (i.e. $F_N > 200$ nN) which might be responsible for its stability against rupture. This result can be explained with the fact that the horizontal wrinkle represents a post-bending configuration of the vertical one, hence similar friction, but the topology of the first had a better time to relax and conform to the basal plane, hence higher stability is achieved at high normal loads.

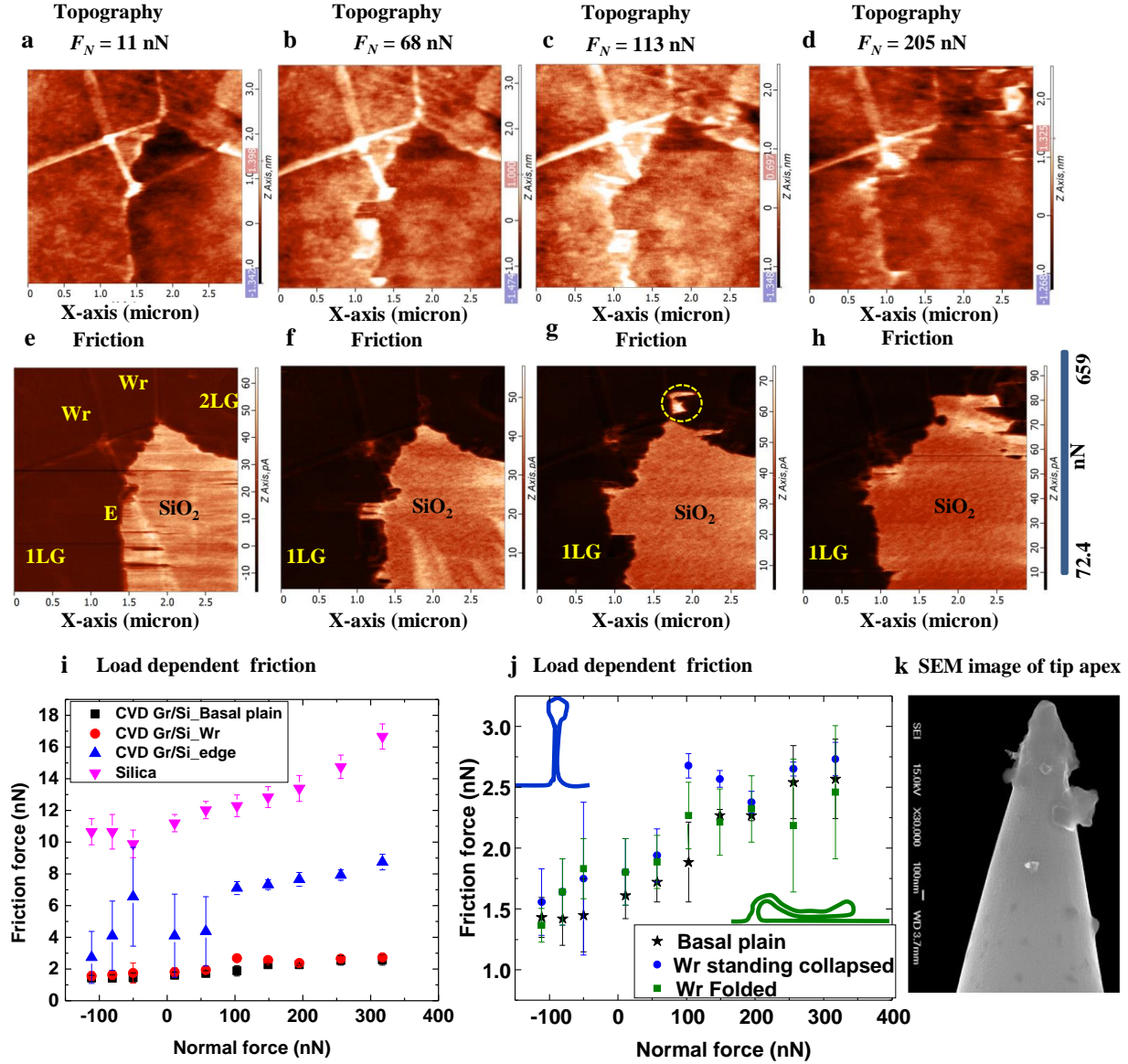
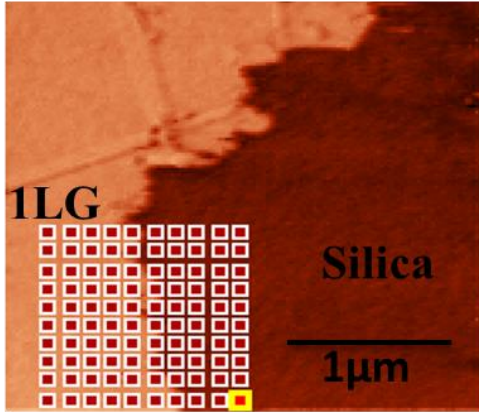


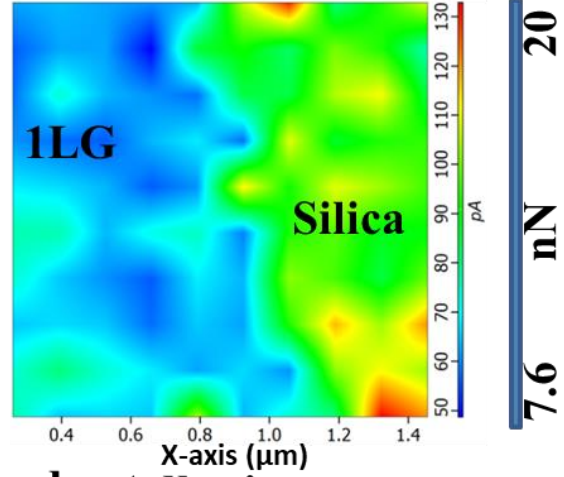
Figure 5: Topography, friction force maps and dependence on normal load for E and horizontal and vertical Wr in CVD graphene. (a-d) AFM topography of CVD graphene over silica substrate at different applied loads. (e-h) Corresponding friction maps. The manipulation of graphene initiates from the E region and progresses up to the rupturing of Wr . (i) Load dependent friction curve showing the trend of F_F at different F_N ; silica substrate shows the highest F_F values while defect free basal graphene plane ($1LG$) has lowest F_F with intermediate values from the E and Wr . (j) Load dependent friction of Wr of standing collapsed and folded wrinkle; the data from $1LG$ basal plane graphene is used for the comparison under same F_N . (k) SEM image of the DLC tip after wear of the graphene sheet showing few graphene debris attached to the tip.

The adhesion force map measured from the silica substrate to the 1LG basal plain are reported in fig.6 at two different regions showing higher values of adhesion force at the *E* region than 1LG. The measurement was carried out with force-distance spectroscopy by calculating pull-out forces. The average value of adhesion force for 1LG is measured as 9.18 ± 2.2 nN and at *E* region is 13 ± 2 nN. A hydrophilic surface like silica has higher affinity to deposit air-borne impurities and attract moisture (i.e. water molecules) responsible for the higher adhesion force at the *E*. Therefore, at the proximity of the *E*, carbon atoms of graphene have a stronger interaction with the sliding probe¹¹ than basal plane graphene leading to higher magnitude of friction as compared to 1LG and 2LG¹¹. The absence of hexagonal symmetry at the *E* regions which make it mechanically vulnerable in friction operations that leads to elastic strain, wrinkle formation, peeling and fracture induced peeling¹⁹. Deng *et al.*² observed significant contrast for the friction and adhesion forces for graphene-silica system for both diamond and silica cantilevers. We observed similar frictional behavior for the CVD as well as for the ME graphene [figure](#) (S3-S5). The obtained friction data are in close agreement and with the measurements carried by Vasic *et al.*¹⁹. The influence of air-borne impurities induced friction is also studied by a separate friction measurement in controlled nitrogen atmosphere complemented with FEM simulation ([figure](#) S6). We obtained lower values of friction force in nitrogen conditions with respect to the air which validates the role of airborne impurities.

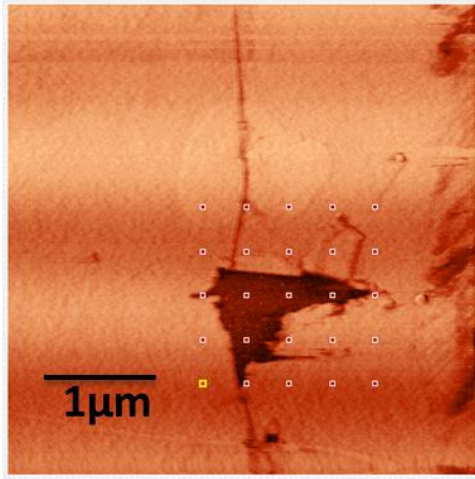
a 100 sampling points



b Adhesion Map



c 25 sampling points



d Adhesion map

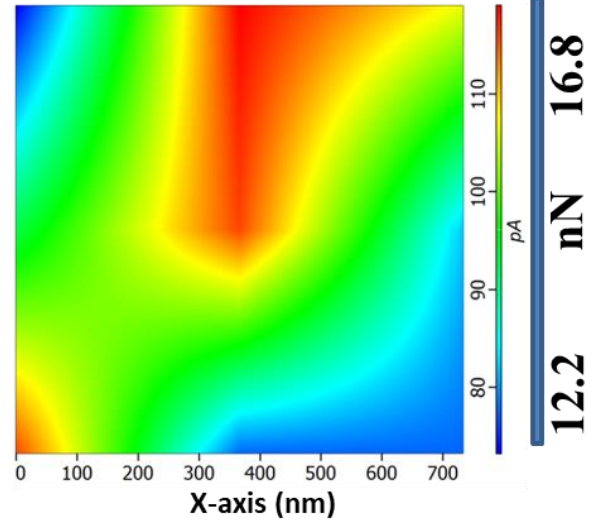


Figure 6: (a, b) Adhesion force map of 100 sampling points carried out over CVD graphene from silica substrate to 1LG. (c, d) Adhesion force map by interpolation of 25 sampling points of silica substrate surrounded by graphene. The color map shows the distribution of adhesion force which is highest at the silica region and lowest in 1LG. Scale bar shows the conversion from pA to nN units using data from the pull-off force.

The trend of load dependent friction in fig 3c and 5i (justifying vanishing F_f at negative values of F_N) is well described according to the following classical law⁴⁰:

$$F_f = \mu(F_N + F_A) + F_{f0} \quad (1)$$

where, μ is the friction coefficient ($\frac{dF_F}{dF_N}$), F_a is the “adhesion” force between the tip apex and graphene measured from pull-out values and F_{F0} is the friction force recorded for $F_N + F_A = 0$ nN. The coefficient of friction (COF) values measured by linear fit of the F_F vs F_N curves of the structural defects are normalized by COF value measured from its corresponding *1LG* and are summarized in table 1. It clearly shows a trend in frictional characteristics of the structural defects depending on chemistry of the tip, shapes (see [figure S7](#)) and the vital role of atmospheric conditions to influence COF values. All measurements are showing *E* is the most vulnerable in air conditions than *SE* and the *Wr* regions, while *2LG* can bear the maximum normal force.

Table 1: The COF values from silica substrate, *E*, *SE* and *Wr* normalized by COF data obtained from its corresponding defect free *1LG* of graphene in air conditions for different probes and related FEM predictions (assuming absence of air borne impurities, thus closer to nitrogen conditions).

| COF _{sample} /COF <i>1LG</i> | DLC probe (air) | Si Probe (air) | Si Probe (Nitrogen) | FEM |
|--|-----------------------|-------------------|------------------------|------|
| Silica substrate/ <i>1LG</i> | 5.33 | 13.46 | 9.78 | - |
| <i>E</i> / <i>1LG</i> | 4 | 3.84 | 1.30 | 1.46 |
| <i>SE</i> / <i>1LG</i> | 1.63 | 2.30 | 0.8 | 0.78 |
| <i>Wr</i> / <i>1LG</i> | 0.66 | 2.25 | - | - |
| <i>2LG</i> / <i>1LG</i> | 0.65 | 0.4 | 0.64 | 0.69 |

Molecular dynamics simulation has been implemented to investigate the mechanical response of the step edge with different range of normal force (F_{NS}) from 45-82 nN, fig. 7a,b and from 80nN-128nN, 7c,d. The simulation set-up is described in the Methods section and the top view of the set-up is given in [figure S8 in](#) supplementary section. The normal force in the simulation F_{NS} is controlled by managing the vertical separation from the surface atoms of graphene. In the subsequent stage of sliding, the probe and graphene terrace shows lower friction force (F_{FS}) than at step edge, see a1 in fig. 7a. The friction is further increased due to a higher interaction of the tip atoms with the step edge, see b1 in fig. 7a, that led to resistance from the step edge atoms. Under given load range, the probe caused elastic folding of the graphene step edge, c1 in fig. 7a. Thus, enhanced friction force was generated due to out-of-plane deformation (see vertical height, fig. 7) counteracting the van der Waals interaction between graphene sheets (i.e. between *1LG* and *2LG*). Folding at c1, fig. 7a, initiates for $F_{NS} = 81.3$ nN and $F_{FS} = 39.6$ nN. The friction decreased when the contact point of the probe passed over the folded step edge atoms. At higher normal force range ($F_{NS} \approx 80$ nN to 128nN, see fig. 7c, d), the probe displaced the graphene *SE*, which in turn generates a buckled structure in in the *SE* region. The friction forces at the buckled *SE* regions is nearly 2.5 times higher than *1LG* basal plain.

The simulation set-up comprises rigid boundary atoms which are artificially fixed and acted as the strained site. Hence, one can obtain the different value of F_{FS} by changing the boundary conditions or its confinement which affect the topography of the basal plane (see fig. S8). Nevertheless, our simulation results illustrate the buckling mechanism followed by the displacement of step edge atoms might be a precursor mechanism for causing tearing at the step edge graphene (see supplementary video SV). Quantitative measure of the structural defect opposition to the lateral movement of the probe is the cumulative work of the probe during its sliding motion, determined as follows:

$$W = \frac{1}{2} \sum_{j=1}^n (L_i + L_{i-1}) (x_i - x_{i-1}) \quad (2)$$

where, L_j is the lateral force corresponding to the X_j displacement of the probe. For fig. 7a it is calculated as 0.564 KeV whereas for fig. 7c is 1.153 KeV. This result shows that the work carried out by the probe to fold graphene step atoms is half the value for buckling and tearing.

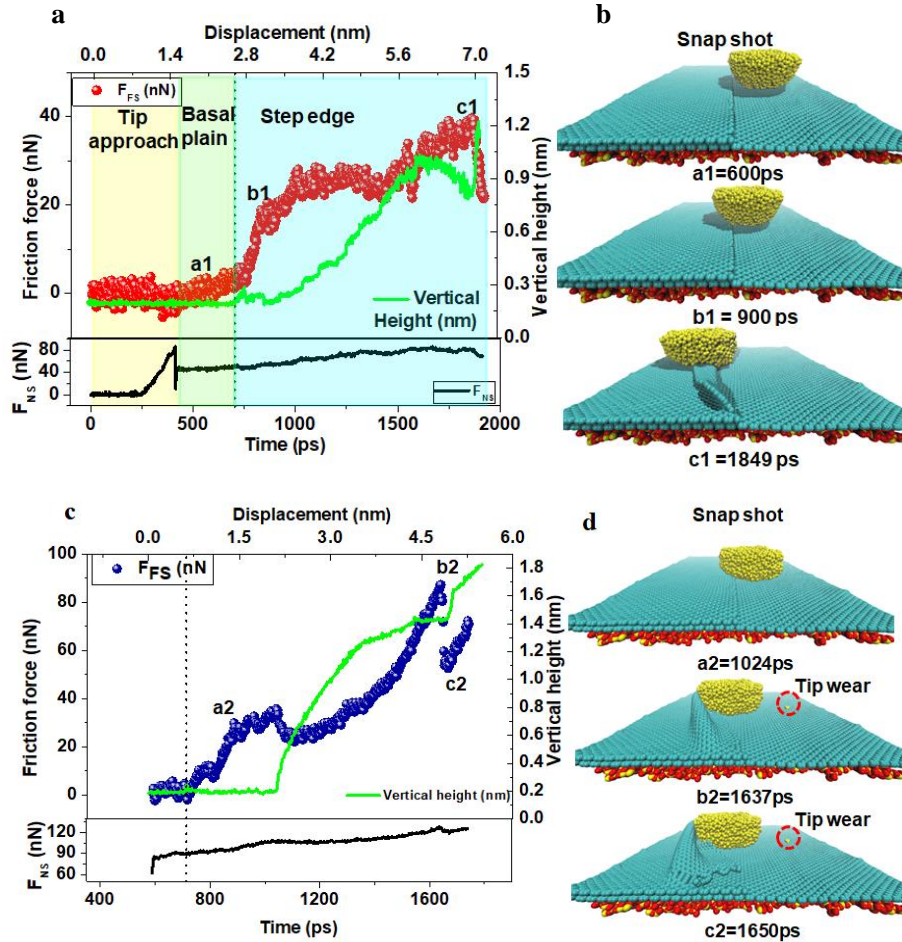


Figure 7: MD simulated friction force profiles and related configurations of SE scanning at two different normal force ranges. The vertical dashed lines identify the position of the E. (a) In the lower panel normal force range elastic folding of the *SE* during tip interaction is observed. (b) Snap shots of three conditions a1, b1 and c1 (folding initiation) given in panel (a). (c) At the higher normal force range “buckling” (starting just after a2) followed by tearing (at b2) of *SE* are observed. After tearing, the friction force drops (b2 to c2). (d) Snap shots of the three conditions a2, b2 and c2 given in panel (d), also showing tip wear.

Conclusion

The structural defects, namely *E*, *SE*, and *Wr* were scanned through AFM at different normal force in both *ME* and *CVD* graphene samples. Lateral deformation appeared higher at the *E* than at the *SE* regions for the *ME* graphene. The deformation phenomenon may yield into folding, buckling and tearing, according to load conditions and defect type as demonstrated by MD and FEM simulations. The *1LG* exhibited *SE* normal forces up to $F_N=74$ nN while wear initiated at the *E* at around $F_N= 57$ nN. It is shown that the basal layer of graphene significantly contributes in the load and friction bearing capacity of a line defect. Airborne impurities might enhance the interaction between probe apex and the *SE* atoms, affecting friction measurements. Normalized COF values from the structural defects with respect of *1LG* quantify a trend of higher COF values from *E* and *SE*. All these factors lead to the detrimental effect on loading bearing capacity of the *E* and *SE* regions. Nevertheless, the role of impurities and its effect on the tribological characteristics of such defects is worthy for further investigations.

In *CVD* graphene, horizontal *Wr* was found to be more robust than vertical ones, whereas the *E* was the weakest against friction and normal forces. For *Wr*, the initiation of the wear appears at the interface between *1LG* and *Wr*. Using DLC and Si tips, we found that the *CVD* graphene is better as a protective coating under sliding operation than *ME* graphene, due to the minimal presence of *E* and *SE* in the former category.

Materials and Methods:

Natural graphite was used as a source of graphene layers, which is mechanically peeled off through scotch tape method and physically deposited over silica substrate (300 nm oxide layer). The produced sample is annealed in Argon atmosphere at 450°C for 3 hours to remove organic impurities. The number of atomic layers of graphene were determined through Raman spectroscopy (Horiba, Jobin-Yvon spectrometer model: Labram, 632.8 nm wavelength, spot diameter ~3-4 μm). *CVD* graphene over silicon sample (Gr/Si-CVD) was commercially obtained from Graphenea (Graphenea Inc., Spain).

AFM measurements in nitrogen condition were carried out as follows: the graphene sample was inserted into an AFM set-up (commercial Enviroscope system by VEECO) with optional sample heater

(Enviroscope P/N: ESHTH), controlled by the Nanoscope IV unit. The AFM chamber is connected with a turbomolecular pump and an oil-free scroll vacuum pump to carry out measurements in high vacuum (10^{-5} Torr). The sample was heated inside the AFM chamber at 150°C for two hours in vacuum. After the cooling of the AFM chamber in vacuum, Nitrogen flux is introduced into the AFM chamber to carry out FFM measurement in Nitrogen atmosphere. FFM measurement was also carried out in air condition using Solver P47H from NT-MDT in contact mode operation using lateral force channel for forward and backward direction.

Commercially available silicon tips PFQNE_AL from Bruker, (MikroMasch model No. CSC37/noAl, NT-MDT model No. CSG01, NSG10, and DCP01 (Silicon probe coated with diamond-like coating) have been used for the topographic analysis and friction measurements. Force-distance (F-D) curves were carried out over Si wafer to measure the sensitivity of the photodetector that allows conversion of units from volts/Ampere to nanometers using the slope of the forward part of curve. The comprehensive detail of the procedure can be found elsewhere⁴¹. The cantilevers were calibrated by following *Sader method*⁴²⁻⁴³ to measure normal and lateral spring constant of the cantilevers. The bending and torsional elastic stiffness of the cantilever were measured $\sim 0.4\text{ N/m}$ and $(2-3) \cdot 10^{-8}\text{ Nm}$, respectively. Lateral force (F_L) is derived from the twisting of cantilever during scanning which is deduced from the lateral photodetector voltage following the procedure described in these articles^{41, 44} with the assumption of the circular shape of laser beam on the photo detector. We refer F_F values as the spatial mean of F_L recorded after scanning of tip in forward and reverse direction. In that calculation, lateral sensitivity of photodetector was assumed to be equal to the sensitivity measured in normal bending of cantilever.

Before performing FFM measurement, the sample was mechanically cleaned in the AFM in contact mode by a different cantilever. Three different graphene flakes has been used for air condition for *ME* graphene and four different regions has been explored over polycrystalline sample (Gr/Si-CVD). The FFM measurement was carried out at an area $1 \times 1\text{ }\mu\text{m}^2$ to $3 \times 3\text{ }\mu\text{m}^2$ while systematically increasing normal force. This procedure allowed to analyze *1LG*, *2LG*, *SE* and silica in the same acquisition and useful to carry out comparative studies. After each session of the FFM, *F-D* curves was performed for pull-off measurements and later cantilevers were passed through silicon grating sample (model no. TGT1) to monitor the shape of the tips.

SEM (scanning electron microscopy) were carried out over Gr/Si-CVD sample using NOVA Instrument operated in SED mode in 10KV.

The finite element simulation model has been developed in order to reproduce a continuous scan from substrate to *2LG* passing through *E* and *SE*. The substrate and the tip are modelled with solid elements while the graphene flake via shell elements (thickness of one layer = $0.066\text{ nm} = 0.34/5$ to properly account bending stiffness of the layer⁴⁵). Van der Waals interaction between all the bodies of the model (tip with flake and substrate, flake and substrate, graphene layers) are modelled via a cohesive zone model based on the Lennard-Jones 6-12 potential⁴⁶. The tip, subjected to imposed F_N can slide in the *xy* plane and a constant translational velocity is imposed in the *X* direction (rotation of the tip is not

permitted). Friction coefficient is determined by computing the x component of the contact force on the tip ($F_L = F_F$).

The molecular dynamic simulations were carried out using the ReaxFF forcefield⁷ implemented in the LAMMPS package¹² at 300K using a time step of 0.5fs. The tip is made by 4099 silicon atoms packed in a $\sim 30\text{\AA}$ radii hemisphere. Its top part (1171 atoms) was considered as a rigid body while its bottom part (2928 atoms) contains atoms that can move freely. The tip was moved using three different springs which are attached in one extremity to the center of mass of the rigid body and in another extremity to a point on the x, y and z axes. The spring constant is 500 Kcal/(mol $\cdot\text{\AA}^2$) in the plane (x and y) and 800 Kcal/(mol $\cdot\text{\AA}^2$) in the vertical (z). Moving the attachment point with a constant velocity ($0.5\times 10^{-5}\text{nm/fs}$ in our simulations) allowed us to measure the interaction force between the tip and the surface in a direction which corresponds to the experienced force by the spring in that direction. To avoid the rotation of the tip, its angular momentum was set to zero at every simulation step. The silica substrate is formed by ~ 11000 atoms packed in $150\text{\AA} \times 150\text{\AA} \times 20\text{\AA}$ flake which was first minimized and then thermalized using the NVT ensemble for 400ps. After that, the graphene sheet formed by ~ 13000 atoms was mounted on the substrate and thermalized for 400ps using NPT ensemble keeping the external pressure null in the periodic direction to avoid any kind of initial stress. Due to the network mismatch between the graphene sheet and the substrate, the substrate was built slightly shorter than the graphene sheet. The silicon tip was minimized and thermalized in the NVT ensemble for 400ps. Then, the simulation begins using the NVT ensemble and keeping the silica substrate and the graphene borders fixed. First, the tip starts to lower down toward substrate until the desired normal force achieved between the tip and the surface. Sequentially, the tip starts to move orthogonally to the edge axis. In MD simulations, we fixed the border to prevent translation of the graphene sheet under the force of the tip. This translation is prevented in the experiments by interactions between graphene and the substrate, in regions where graphene is not suspended (simulating this entire setup is beyond the capabilities of computational infrastructure are not needed here). By reducing the size of the graphene flake, we also accelerate the entire duration of fracture process. We observed good agreement between results from simulations and experiments regarding the friction forces.

Supporting Information

Thickness measurement and roughness distribution of *ME* and *CVD* graphene by AFM (intermittent contact mode), SEM, Raman spectroscopy. Friction profile using Si and DLC probe at fixed load and load dependent friction curves. Mechanical cleaning of graphene to remove air borne impurities and conformation of graphene flake with silica substrate. Friction and adhesion map of different *ME* graphene flakes. Kelvin Probe force microscopy to show the distribution of charges around structural defects for *ME* and *CVD* graphene. Intermittent contact mode image of torn graphene from the edge as well as from the step edge after FFM measurements. Adhesion map of *CVD* graphene after tearing. Set-up of molecular dynamics simulation from 1LG-2LG over Si substrate. The Supplementary Videos shows the different phenomena of deformation of the step edge region under different applied force.

Acknowledgements

NMP is supported by the European Commission with the Graphene Flagship Core 2 n. 785219 (WP14 “Composites”) and FET Proactive “Neurofibres” n. 732344 as well as by the MIUR with the “Departments of Excellence” grant L. 232/2016 and ARS01-01384-PROSCAN. MT like to thank Mario Barozzi for providing SEM images. GP and SV like to acknowledge Regione Emilia Romagna, Project INTERMECH–MO.RE and EU COST program under Action MP1303. FA would like to acknowledge the financial support of the FWF Lise Meitner program, project M1777. SS acknowledges financial support from Ermenegildo Zegna Founder’s Scholarship 2017.

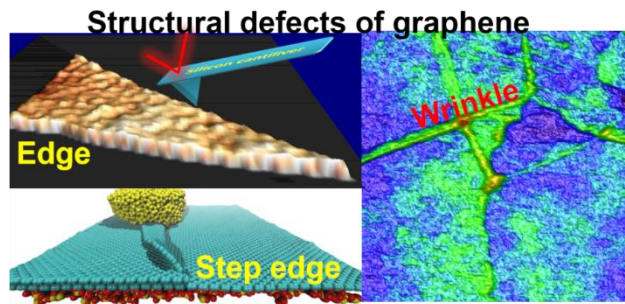
References

- (1) Feng, X.; Kwon, S.; Park, J. Y.; Salmeron, M. Superlubric Sliding of Graphene Nanoflakes on Graphene. *ACS nano* **2013**, 7 (2), 1718-1724, DOI: 10.1021/nn305722d.
- (2) Deng, Z.; Klimov, N. N.; Solares, S. D.; Li, T.; Xu, H.; Cannara, R. J. Nanoscale Interfacial Friction and Adhesion on Supported versus Suspended Monolayer and Multilayer Graphene. *Langmuir* **2013**, 29 (1), 235-243, DOI: 10.1021/la304079a.
- (3) Klemenz, A.; Pastewka, L.; Balakrishna, S. G.; Caron, A.; Bennewitz, R.; Moseler, M. Atomic Scale Mechanisms of Friction Reduction and Wear Protection by Graphene. *Nano Letters* **2014**, 14 (12), 7145-7152, DOI: 10.1021/nl5037403.
- (4) Wählich, F.; Hoth, J.; Held, C.; Seyller, T.; Bennewitz, R. Friction and atomic-layer-scale wear of graphitic lubricants on SiC(0001) in dry sliding. *Wear* **2013**, 300 (1–2), 78-81, DOI: <http://dx.doi.org/10.1016/j.wear.2013.01.108>.
- (5) Shin, Y. J.; Stromberg, R.; Nay, R.; Huang, H.; Wee, A. T. S.; Yang, H.; Bhatia, C. S. Frictional characteristics of exfoliated and epitaxial graphene. *Carbon* **2011**, 49 (12), 4070-4073, DOI: 10.1016/j.carbon.2011.05.046.
- (6) Kim, K. S.; Lee, H. J.; Lee, C.; Lee, S. K.; Jang, H.; Ahn, J. H.; Kim, J. H. Chemical vapor deposition-grown graphene: the thinnest solid lubricant. *ACS nano* **2011**, 5 (6), 5107-5114, DOI: 10.1021/nn2011865.
- (7) Sandoz-Rosado, E. J.; Tertuliano, O. A.; Terrell, E. J. An atomistic study of the abrasive wear and failure of graphene sheets when used as a solid lubricant and a comparison to diamond-like-carbon coatings. *Carbon* **2012**, 50 (11), 4078-4084, DOI: <http://dx.doi.org/10.1016/j.carbon.2012.04.055>.
- (8) Vasić, B.; Zurutuza, A.; Gajić, R. Spatial variation of wear and electrical properties across wrinkles in chemical vapour deposition graphene. *Carbon* **2016**, 102, 304-310, DOI: <http://dx.doi.org/10.1016/j.carbon.2016.02.066>.
- (9) Long, F.; Yasaei, P.; Yao, W.; Salehi-Khojin, A.; Shahbazian-Yassar, R. Anisotropic Friction of Wrinkled Graphene Grown by Chemical Vapor Deposition. *ACS Applied Materials & Interfaces* **2017**, 9 (24), 20922-20927, DOI: 10.1021/acsami.7b00711.
- (10) Huang, P. Y.; Ruiz-Vargas, C. S.; van der Zande, A. M.; Whitney, W. S.; Levendorf, M. P.; Kevek, J. W.; Garg, S.; Alden, J. S.; Hustedt, C. J.; Zhu, Y.; Park, J.; McEuen, P. L.; Muller, D. A. Grains and grain boundaries in single-layer graphene atomic patchwork quilts. *Nature* **2011**, 469 (7330), 389-392, DOI: 10.1038/nature09718.
- (11) Lee, H.; Lee, H.-B.-R.; Kwon, S.; Salmeron, M.; Park, J. Y. Internal and External Atomic Steps in Graphite Exhibit Dramatically Different Physical and Chemical Properties. *ACS nano* **2015**, 9 (4), 3814-3819, DOI: 10.1021/nn506755p.
- (12) Zhang, J.; Zhao, J.; Lu, J. Intrinsic Strength and Failure Behaviors of Graphene Grain Boundaries. *ACS nano* **2012**, 6 (3), 2704-2711, DOI: 10.1021/nn3001356.
- (13) Ruiz-Vargas, C. S.; Zhuang, H. L.; Huang, P. Y.; van der Zande, A. M.; Garg, S.; McEuen, P. L.; Muller, D. A.; Hennig, R. G.; Park, J. Softened Elastic Response and Unzipping in Chemical Vapor Deposition Graphene Membranes. *Nano Letters* **2011**, 11 (6), 2259-2263, DOI: 10.1021/nl200429f.
- (14) Han, J.; Pugno, N. M.; Ryu, S. Nanoindentation cannot accurately predict the tensile strength of graphene or other 2D materials. *Nanoscale* **2015**, 7 (38), 15672-15679.

- (15) Androulidakis, C.; Koukaras, E. N.; Frank, O.; Tsoukleri, G.; Sfyris, D.; Parthenios, J.; Pugno, N.; Papagelis, K.; Novoselov, K. S.; Galiotis, C. Failure processes in embedded monolayer graphene under axial compression. *Scientific reports* **2014**, *4*, [5271](#).
- (16) Pugno, N. M. The elasticity and strength of graphene. *Recent Res. Devel. Mat.Sci* **2009**, *8*, [101-103](#).
- (17) Qi, Z.; Cao, P.; Park, H. S. Density functional theory calculation of edge stresses in monolayer MoS₂. *Journal of Applied Physics* **2013**, *114* (16), 163508, DOI: [doi:http://dx.doi.org/10.1063/1.4826905](http://dx.doi.org/10.1063/1.4826905).
- (18) Suenaga, K.; Koshino, M. Atom-by-atom spectroscopy at graphene edge. *Nature* **2010**, *468* (7327), 1088-1090, DOI: <http://www.nature.com/nature/journal/v468/n7327/abs/nature09664.html#supplementary-information>.
- (19) Vasić, B.; Matković, A.; Gajić, R.; Stanković, I. Wear properties of graphene edges probed by atomic force microscopy based lateral manipulation. *Carbon* **2016**, *107*, 723-732, DOI: <http://dx.doi.org/10.1016/j.carbon.2016.06.073>.
- (20) Lee, C.; Li, Q.; Kalb, W.; Liu, X. Z.; Berger, H.; Carpick, R. W.; Hone, J. Frictional characteristics of atomically thin sheets. *Science* **2010**, *328* (5974), 76-80, DOI: [10.1126/science.1184167](https://doi.org/10.1126/science.1184167).
- (21) Dong, Y.; Liu, X. Z.; Egberts, P.; Ye, Z.; Carpick, R. W.; Martini, A. Correlation Between Probe Shape and Atomic Friction Peaks at Graphite Step Edges. *Tribology Letters* **2012**, *50* (1), 49-57, DOI: [10.1007/s11249-012-0072-z](https://doi.org/10.1007/s11249-012-0072-z).
- (22) Fajardo, O. Y.; Mazo, J. J. Surface defects and temperature on atomic friction. *Journal of physics. Condensed matter : an Institute of Physics journal* **2011**, *23* (35), 355008, DOI: [10.1088/0953-8984/23/35/355008](https://doi.org/10.1088/0953-8984/23/35/355008).
- (23) Meyer, E.; Lüthi, R.; Howald, L.; Bammerlin, M.; Guggisberg, M.; Güntherodt, H. J. Site-specific friction force spectroscopy. *Journal of Vacuum Science & Technology B* **1996**, *14* (2), 1285-1288, DOI: [doi:http://dx.doi.org/10.1116/1.589082](https://doi.org/10.1116/1.589082).
- (24) Overney, R. M.; Meyer, E.; Frommer, J.; Brodbeck, D.; Luthi, R.; Howald, L.; Güntherodt, H. J.; Fujihira, M.; Takano, H.; Gotoh, Y. Friction measurements on phase-separated thin films with a modified atomic force microscope. *Nature* **1992**, *359* (6391), 133-135.
- (25) Egberts, P.; Han, G. H.; Liu, X. Z.; Johnson, A. T. C.; Carpick, R. W. Frictional Behavior of Atomically Thin Sheets: Hexagonal-Shaped Graphene Islands Grown on Copper by Chemical Vapor Deposition. *ACS nano* **2014**, *8* (5), 5010-5021, DOI: [10.1021/nn501085g](https://doi.org/10.1021/nn501085g).
- (26) Ye, Z.; Martini, A. Atomic friction at exposed and buried graphite step edges: experiments and simulations. *Applied Physics Letters* **2015**, *106* (23), 231603.
- (27) Yu, S. U.; Park, B.; Cho, Y.; Hyun, S.; Kim, J. K.; Kim, K. S. Simultaneous visualization of graphene grain boundaries and wrinkles with structural information by gold deposition. *ACS nano* **2014**, *8* (8), 8662-8668.
- (28) Cannara, R. J.; Brukman, M. J.; Cimat, K.; Sumant, A. V.; Baldelli, S.; Carpick, R. W. Nanoscale friction varied by isotopic shifting of surface vibrational frequencies. *Science* **2007**, *318* (5851), 780-3, DOI: [10.1126/science.1147550](https://doi.org/10.1126/science.1147550).
- (29) Li, Q.; Tullis, T. E.; Goldsby, D.; Carpick, R. W. Frictional ageing from interfacial bonding and the origins of rate and state friction. *Nature* **2011**, *480* (7376), 233-236, DOI: <http://www.nature.com/nature/journal/v480/n7376/abs/nature10589.html#supplementary-information>.
- (30) Weymouth, A. J.; Hofmann, T.; Giessibl, F. J. Quantifying Molecular Stiffness and Interaction with Lateral Force Microscopy. *Science* **2014**, *343* (6175), 1120-1122.
- (31) Dietzel, D.; Mönninghoff, T.; Herding, C.; Feldmann, M.; Fuchs, H.; Stegemann, B.; Ritter, C.; Schwarz, U. D.; Schirmeisen, A. Frictional duality of metallic nanoparticles: Influence of particle morphology, orientation, and air exposure. *Physical Review B* **2010**, *82* (3), 035401, DOI: [10.1103/PhysRevB.82.035401](https://doi.org/10.1103/PhysRevB.82.035401).
- (32) Ternes, M.; Lutz, C. P.; Hirjibehedin, C. F.; Giessibl, F. J.; Heinrich, A. J. The Force Needed to Move an Atom on a Surface. *Science* **2008**, *319* (5866), 1066-1069, DOI: [10.1126/science.1150288](https://doi.org/10.1126/science.1150288).
- (33) Hölscher, H.; Ebeling, D.; Schwarz, U. D. Friction at Atomic-Scale Surface Steps: Experiment and Theory. *Physical Review Letters* **2008**, *101* (24), 246105.
- (34) Sundararajan, S.; Bhushan, B. Topography-induced contributions to friction forces measured using an atomic force/friction force microscope. *Journal of Applied Physics* **2000**, *88* (8), 4825, DOI: [10.1063/1.1310187](https://doi.org/10.1063/1.1310187).
- (35) Demirbaş, T.; Baykara, M. Z. Nanoscale tribology of graphene grown by chemical vapor deposition and transferred onto silicon oxide substrates. *Journal of Materials Research* **2016**, *31* (13), 1914-1923.

- (36) Malard, L. M.; Pimenta, M. A.; Dresselhaus, G.; Dresselhaus, M. S. Raman spectroscopy in graphene. *Physics Reports* **2009**, *473* (5–6), 51-87, DOI: <http://dx.doi.org/10.1016/j.physrep.2009.02.003>.
- (37) Ye, Z.; Balkanci, A.; Martini, A.; Baykara, M. Z. Effect of roughness on the layer-dependent friction of few-layer graphene. *Physical Review B* **2017**, *96* (11), 115401.
- (38) Filleter, T.; McChesney, J.; Bostwick, A.; Rotenberg, E.; Emtsev, K.; Seyller, T.; Horn, K.; Bennewitz, R. Friction and Dissipation in Epitaxial Graphene Films. *Physical Review Letters* **2009**, *102* (8), [086102](https://doi.org/10.1103/PhysRevLett.102.086102). DOI: 10.1103/PhysRevLett.102.086102.
- (39) Qi, Y.; Liu, J.; Zhang, J.; Dong, Y.; Li, Q. Wear Resistance Limited by Step Edge Failure: The Rise and Fall of Graphene as an Atomically Thin Lubricating Material. *ACS Applied Materials & Interfaces* **2017**, *9* (1), 1099-1106, DOI: 10.1021/acsami.6b12916.
- (40) Gao, J.; Luedtke, W. D.; Gourdon, D.; Ruths, M.; Israelachvili, J. N.; Landman, U. Frictional Forces and Amontons' Law: From the Molecular to the Macroscopic Scale. *The Journal of Physical Chemistry B* **2004**, *108* (11), 3410-3425, DOI: 10.1021/jp036362l.
- (41) Carpick, R. W.; Salmeron, M. Scratching the Surface: Fundamental Investigations of Tribology with Atomic Force Microscopy. *Chemical reviews* **1997**, *97* (4), 1163-1194, DOI: 10.1021/cr960068q.
- (42) Sader, J. E.; Chon, J. W. M.; Mulvaney, P. Calibration of rectangular atomic force microscope cantilevers. *Review of Scientific Instruments* **1999**, *70* (10), 3967, DOI: 10.1063/1.1150021.
- (43) Green, C. P.; Lioe, H.; Cleveland, J. P.; Proksch, R.; Mulvaney, P.; Sader, J. E. Normal and torsional spring constants of atomic force microscope cantilevers. *Review of Scientific Instruments* **2004**, *75* (6), 1988, DOI: 10.1063/1.1753100.
- (44) Bachmann, D.; Hierold, C. Determination of pull-off forces of textured silicon surfaces by AFM force curve analysis. *Journal of Micromechanics and Microengineering* **2007**, *17* (7), 1326-1333, DOI: 10.1088/0960-1317/17/7/015.
- (45) Scarpa, F.; Adhikari, S.; Gil, A.; Remillat, C. The bending of single layer graphene sheets: the lattice versus continuum approach. *Nanotechnology* **2010**, *21* (12), 125702.
- (46) Jiang, L. Y.; Huang, Y.; Jiang, H.; Ravichandran, G.; Gao, H.; Hwang, K.; Liu, B. A cohesive law for carbon nanotube/polymer interfaces based on the van der Waals force. *Journal of the Mechanics and Physics of Solids* **2006**, *54* (11), 2436-2452.

For Table of Contents Only



Supplementary Information

Friction and adhesion of different structural defects of graphene

Manoj Tripathi^a, Firas Awaja^b, Rafael A. Bizão^{c,a}, Stefano Signetti^d, Erica Iacob^e, Guido Paolicelli^f, Sergio Valeri^{f,g}, Alan Dalton^a, Nicola Maria Pugno^{a,h,i,*}

^a Department of Mathematics and Physical sciences, University of Sussex, Brighton, BN1 9RH, UK

^b Department of Orthopaedic Surgery, Medical University Innsbruck, Innrain 36, Innsbruck, Austria

^c Applied Physics Department, State University of Campinas, Campinas-SP, 13083-959, Brazil

^d Department of Mechanical Engineering, Korea Advanced institute of Science and Technology (KAIST), 291 Daehak-ro, Yuseong-gu, Daejeon 34141, Republic of Korea

^e Centre for Materials and Microsystems, Fondazione Bruno Kessler, via Sommarive 18, I-38123 Trento, Italy

^f Istituto Nanoscienze, Consiglio Nazionale delle Ricerche, via G. Campi 213/a, 41125- Modena, Italy

^g Dipartimento di Scienze Fisiche Informatiche e Matematiche (FIM), Università di Modena e Reggio Emilia, Via Campi 213/a, I-41125 Modena, Italy

^h School of Engineering and Materials Science, Queen Mary University of London, Mile End Road, E1 4NS London - United Kingdom

ⁱ Ket Lab, Edoardo Amaldi Foundation, Italian Space Agency, Via del Politecnico snc, I-00133 Roma, Italy

Supplementary Information

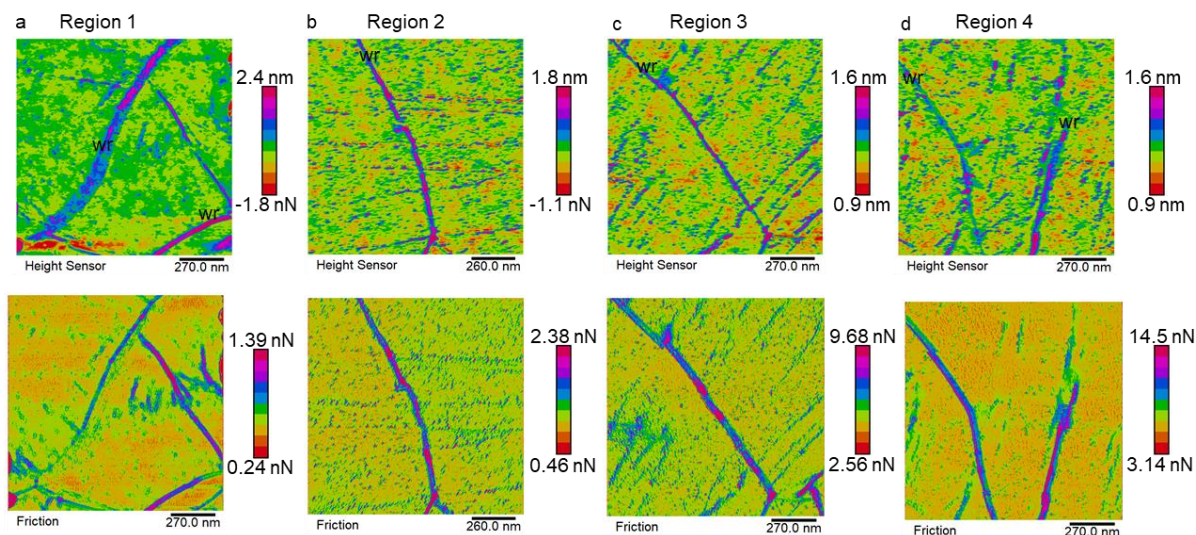


Figure S1: Topography (upper row) and frictional force (lower row) characteristics of the graphene wrinkle as compared to its surrounded graphene basal plain obtained at different locations from different cantilevers. The cantilever of stiffness $K_n = 1.3$ N/m for the panel (a) and (b) and $K_n = 2.6$ N/m for the panel (c) and (d) were used for the friction force measurements. The applied normal force is slightly increasing from panel (a) to panel (d). Wrinkles of different altitude, orientation and width show a contrast

in friction force as compared to its surrounding graphene. The scale bar clearly differentiates the higher altitude of the wrinkle responsible for the larger friction force to the cantilevers.

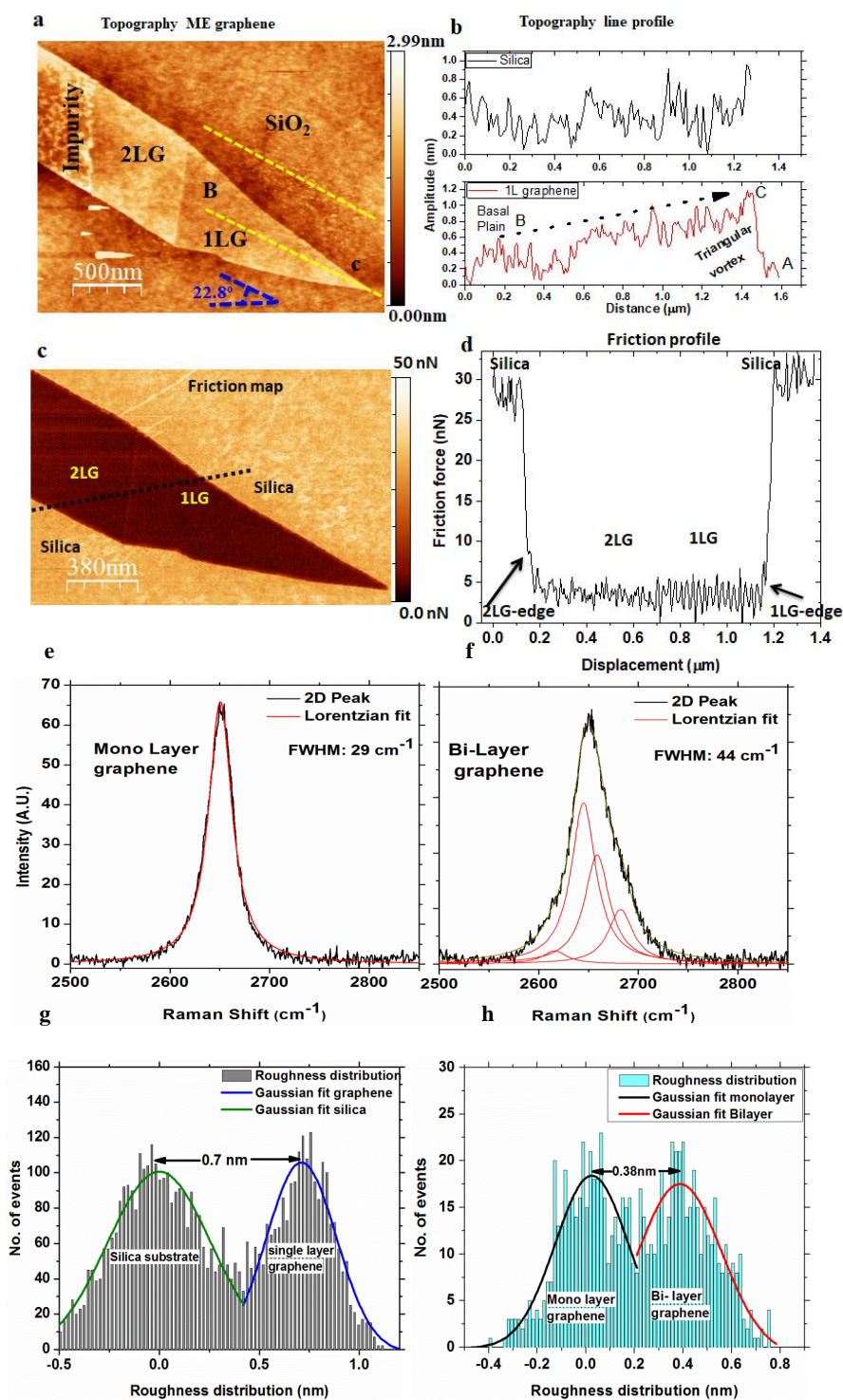


Figure S2: (a) AFM topographic image (intermittent contact mode) of *ME* graphene after mechanical cleaning in contact mode operation. The bright color in AFM topography represents elevated graphene from the substrate. This is validated by line profile over silica surface parallel to the axis of the graphene sheet. The altitude of *1LG* is increasing from the basal plane (B) to the vertex (C) from 0.2 to 1.2 nm and drop again at point A (silica substrate). (b) Topography profile of silica surface parallel to the line profile on *1LG* shows constant height, thus the absence of any artefact. It shows graphene edge region along the vertex has lower interaction with silica substrate as compared to the basal plane. (c and d) Friction map of *ME* graphene showing friction contrast at the *2LG*, *1LG*, *SE*, and *E* at fixed F_N . Friction line profile along *2LG*-edge to *1LG*-edge showing slight differences in the F_F , which corresponds in altitude to the edge defects. (e and f) Raman spectra of 2D peak for *1LG* ($\sim 2651 \text{ cm}^{-1}$) and *2LG* (2654 cm^{-1}) respectively. The monolayer is fitted with a single Lorentzian curve with the full width half maximum (FWHM) $\sim 29 \text{ cm}^{-1}$ and the bi-layer is fitted with four Lorentzian curves¹. (g and h) Roughness distribution of *1LG* over silica substrate and *1LG-2LG* is used to measure the thickness of graphene layer/s. The Gaussian fit of the roughness distribution shows average altitude difference between *1LG-silica* and *1LG-2LG*, being 0.7 nm and 0.38 nm respectively.

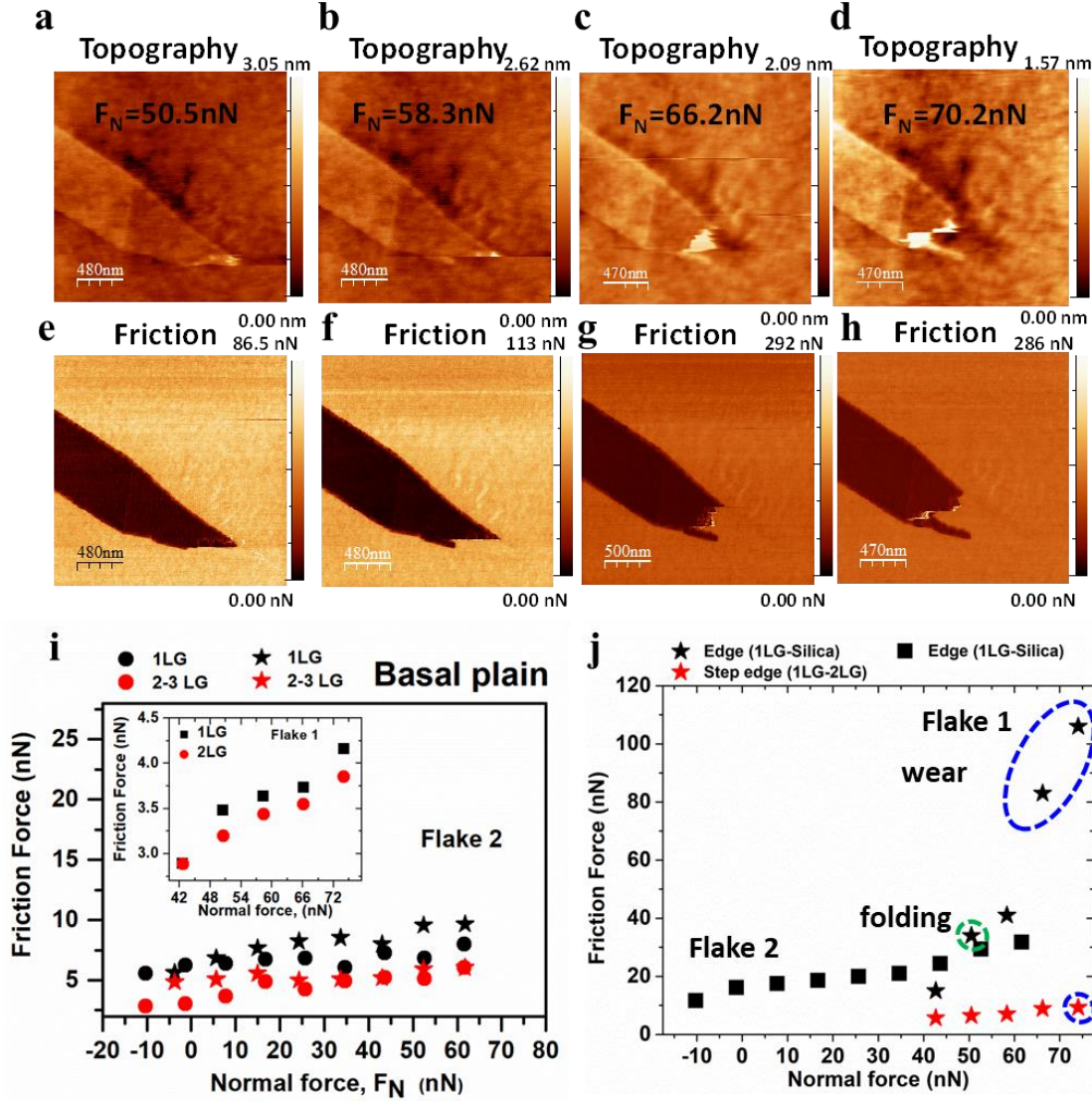


Figure S3: Topography and friction force maps dependence on normal load for *E* and *SE* in *ME* graphene. Manipulation of graphene flakes with increasing normal force from 50 to 70 nN, leading to observations suggesting folding (a) cutting of the folded graphene, (b) tearing and (c, d) wear. The F_F maps are given in panels (e-h). (i) F_F vs F_N for the two different basal plane graphene flakes (no. 1 and 2) for 1LG, and 2LG (repeated twice). 1LG has higher friction force than 2LG for all normal forces. (j) F_F vs F_N for *E* and *SE*, which leads to deformations in graphene flakes, like folding (green dashed circle) and wear (blue dashed circle). The *E* and *SE* regions of *ME* graphene by varying the normal force F_N between 50 to 70 nN. The F_F increases with higher F_N and deformation occurs at the *E* region by folding fig. S2 a, e, cutting b, f and wear d, h phenomena. The friction force from 1LG, 2LG, *SE* and *E* are reported in fig. S2i, j for two different *ME* graphene flakes (flake no. 1 and 2). The 2LG surface shows the lowest friction forces for all applied F_N whereas *E* the highest values. The tearing of *E* is observed at $F_N \approx 58$ nN and for *SE* at ≈ 74 nN.

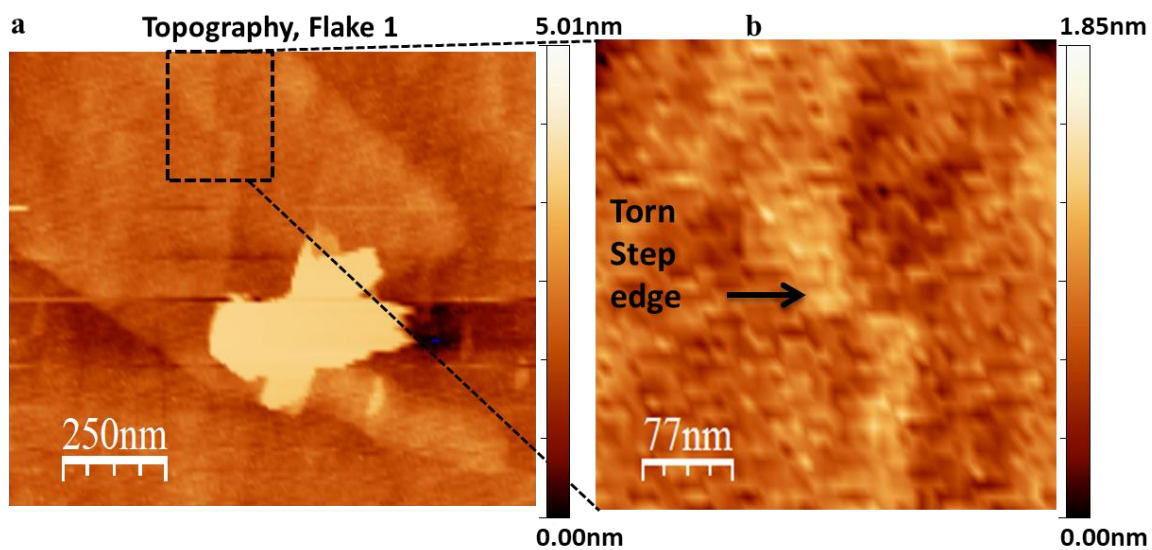


Figure S4. (a) Intermittent contact mode carried out after FFM operations showing rupture of the edge and initiation of tearing at the step-edge for fixed normal load of 74 nN. (b) zoom region around the broken step edge.

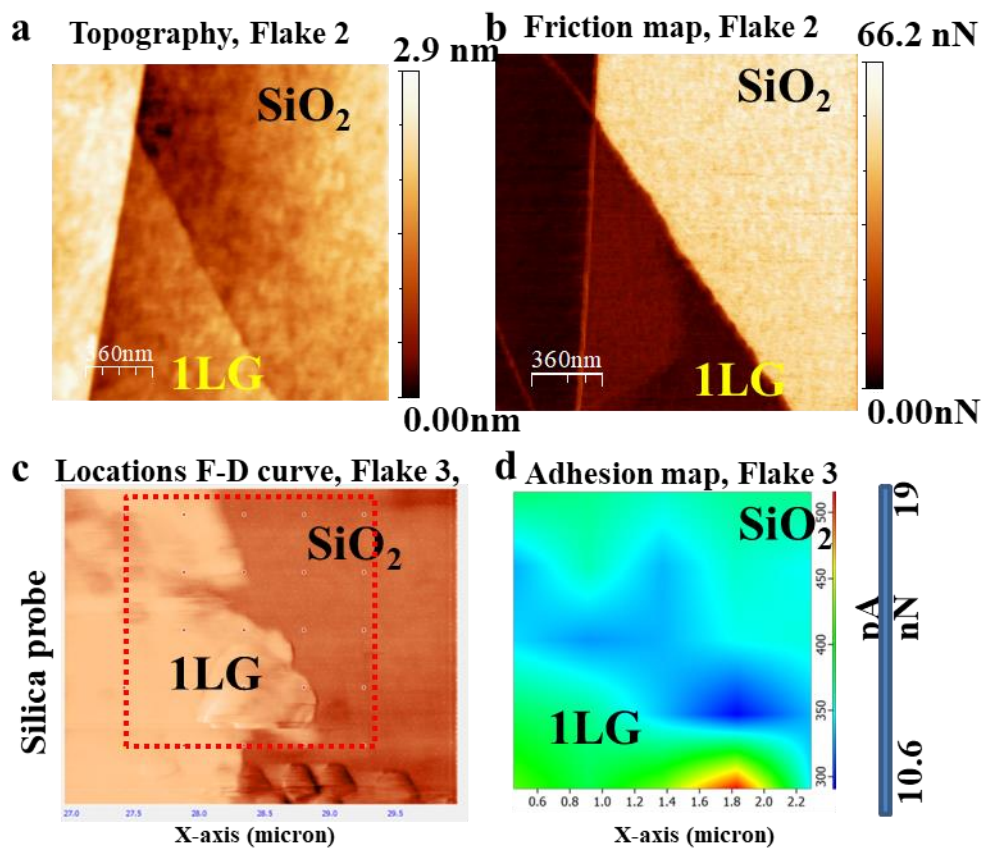


Figure S5: (a, b) Topography and friction force map of *ME* flake no. 2 that include *E* and *SE*. (c, d) Adhesion force map (25 sampling points) has been carried out at the interface between *1LG* and silica substrates by silica probe. The pull-off force map (using re-tract part of the curve) at the interface between graphene edge region and silica shows higher adhesion force at the *1LG* (edge region) than graphene basal plain (*1LG*), indicating the higher affinity of the edge region towards sliding tip.

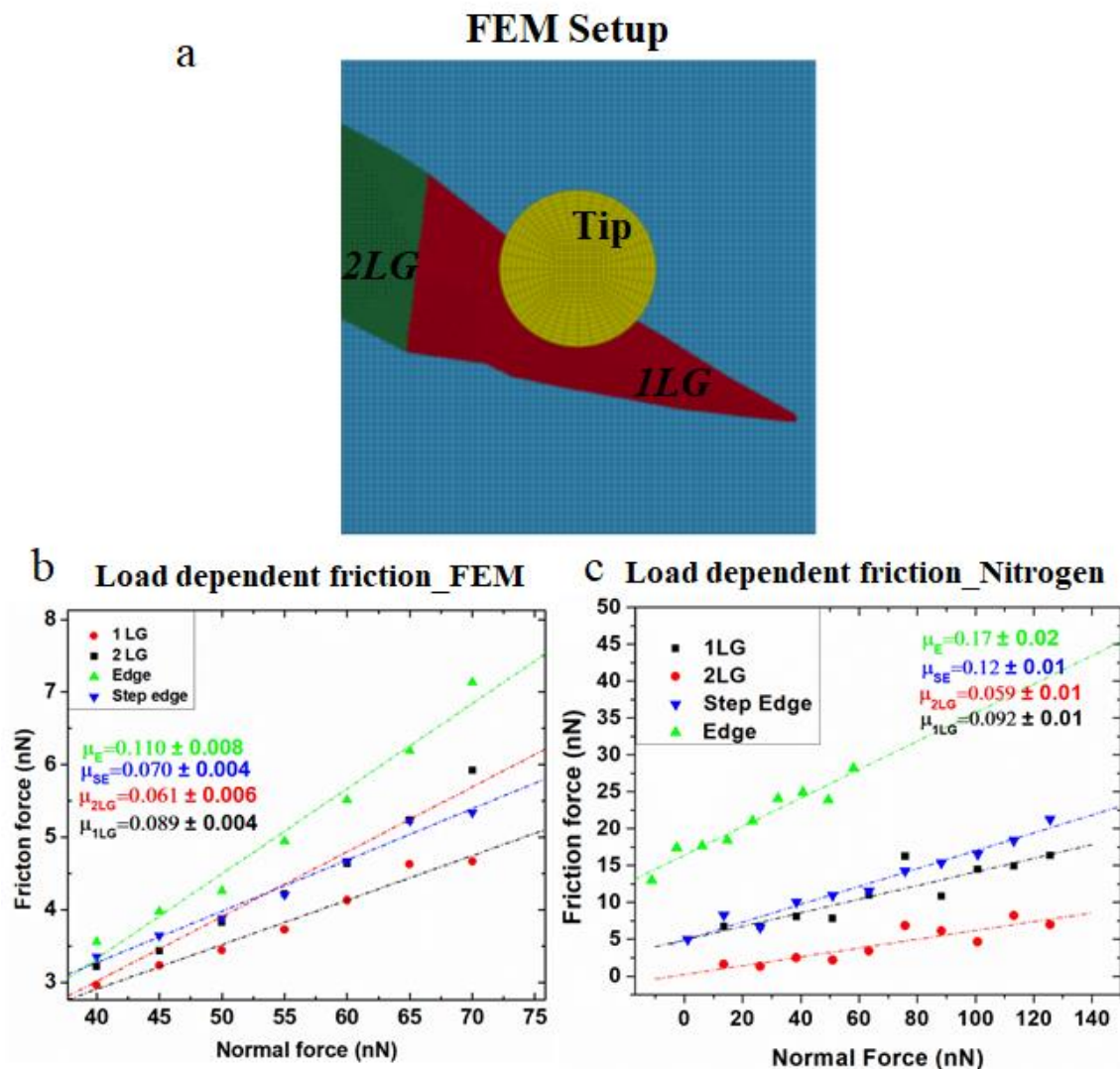


Figure S6: FEM simulation for load dependent friction on *1LG*, *2LG* and experimental FFM measurement in nitrogen atmosphere. (a) Set-up of finite element method (FEM) of *1LG* and *2LG* flake against hemispherical silicon slider. (b) FEM based load dependent friction and COF values measured by linear fit for *1LG* (~0.089) and *2LG* (~0.061), *SE* (~0.07) and *E* (~0.11). (c) Experimental FFM measurement carried out in nitrogen atmosphere are in close agreement with FEM showing COF values nearly 0.092, 0.059, 0.12, 0.17, respectively.

The finite element simulation model has been developed in order to reproduce a continuous scan from silica substrate to *2LG* passing through *E* and *SE* (Figure S5. a). The substrate and the tip are modelled with solid elements while the graphene flake via shell elements. The thickness of graphene was reduced by a factor 5^2 , $t = 0.066 \text{ nm} = 0.34 \text{ nm}/5$, to not overestimate transversal stiffness of the layer and the nominal elastic modulus of graphene (1 TPa) was scaled accordingly in order to preserve membrane stiffness $Et = \text{const}$. The molecular van der Waals interaction between all the bodies of the

model (silica substrate, graphene layers and silica) are modelled via a continuum cohesive zone model based on the Lennard-Jones (LJ) 6-12 potential as derived and described extensively by Jiang et al.³ The cohesive normal stress between graphene layers is expressed as derivative of the variationally cohesive energy per unit area with respect to the nodes separation distance (perturbation) v :

$$\sigma_{\text{cohesive, G/G}} = 8\pi\Psi_C^2 \varepsilon_{\text{C-C}} s_{\text{C-C}} \left(\frac{s_{\text{C-C}}^5}{(h_{\text{G/G}} + v)^5} - \frac{s_{\text{C-C}}^{11}}{(h_{\text{G/G}} + v)^{11}} \right) \quad (\text{S1})$$

where Ψ is the number of graphene atom per unit area, $\varepsilon_{\text{C-C}}$ and $s_{\text{C-C}}$ are the LJ potential parameters for carbon-carbon interaction³, $h_{\text{G/G}} = \sqrt[6]{2s_{\text{C-C}}}$ is the graphene inter-layer equilibrium distance. Note that v corresponds the current node-to-segment separation between contacting interfaces and that the cohesive stress nearly vanishes for $v > 3h_{\text{G/G}}$. On the other hand, the interfacial shear strength associated with van der Waals adhesion has been demonstrated to be negligibly small³, thus $\tau_{\text{cohesive, G/G}} = 0$.

Analogously for the graphene-silica interaction we have:

$$\begin{aligned} \sigma_{\text{cohesive, G/SiO}_2} = & 8\pi\Psi_C \Psi_{\text{Si}} \varepsilon_{\text{C-Si}} s_{\text{C-Si}} \left(\frac{s_{\text{C-Si}}^5}{(h_{\text{G/SiO}_2} + v)^5} - \frac{s_{\text{C-Si}}^{11}}{(h_{\text{G/SiO}_2} + v)^{11}} \right) \\ & + 8\pi\Psi_C \Psi_{\text{O}} \varepsilon_{\text{C-O}} s_{\text{C-O}} \left(\frac{s_{\text{C-O}}^5}{(h_{\text{G/SiO}_2} + v)^5} - \frac{s_{\text{C-O}}^{11}}{(h_{\text{G/SiO}_2} + v)^{11}} \right) \end{aligned} \quad (\text{S2})$$

with

$$h_{\text{G/SiO}_2} = \left(\frac{\varepsilon_{\text{C-Si}} s_{\text{C-Si}}^{12} + \varepsilon_{\text{C-O}} s_{\text{C-O}}^{12}}{\varepsilon_{\text{C-Si}} s_{\text{C-Si}}^6 + \varepsilon_{\text{C-O}} s_{\text{C-O}}^6} \right)^{1/6} \quad (\text{S3})$$

where the LJ parameters were taken from Kumar *et al.*³

Analogously to MD simulation, the tip is subjected to imposed F_N on a surface and translated in the xy plane with a constant velocity towards the SE. Rotations of the nodes of the tip are fixed, thus tilt of the simulated AFM is not permitted. Friction force is determined by computing the component of the contact force on the tip ($F_L = F_F$) parallel to scanning motion and the friction coefficient is determined as $\frac{dF_T}{dF_N}$.

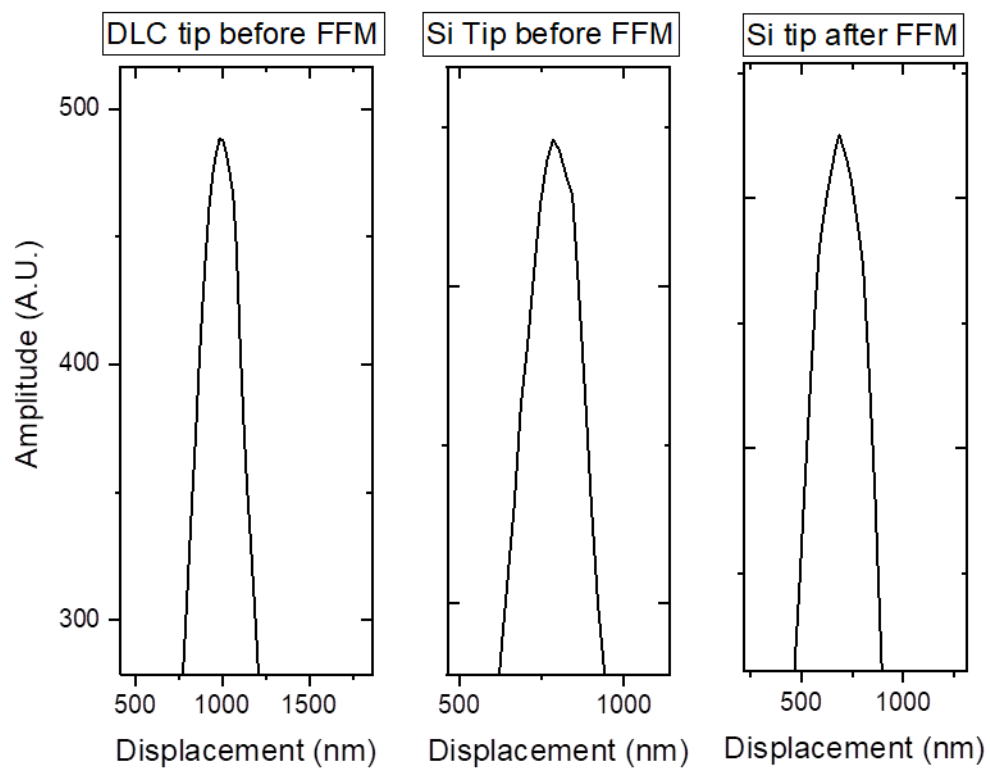


Figure S7: Line profile of different tip apex scanned over the standard grating. The SEM image DLC tip post FFM measurement is inserted in the main text, since grating scanning could remove the graphene flakes around tip apex.

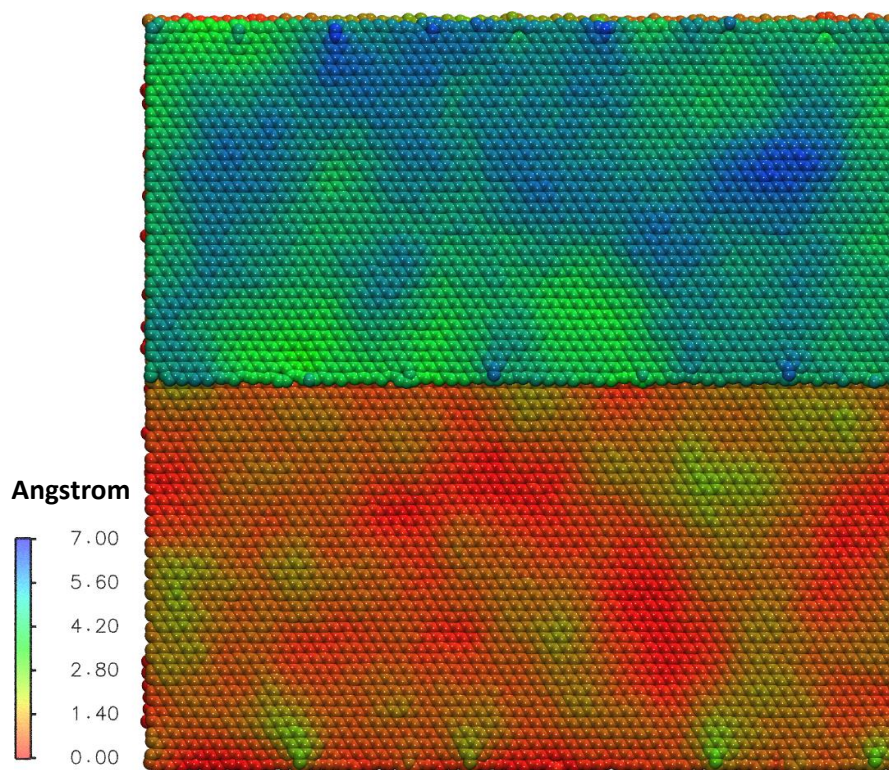


Figure S8. Set-up of MD simulation. Top view of corrugated arrangement of single layer, bi-layer and step-edge atoms. These corrugations were achieved through energy minimization followed by thermalization of the system. The colour distribution is associated with the position of graphene atoms in vertical direction (z) giving a qualitative sight of the corrugation of the graphene layers.

References

1. Gupta, A.; Chen, G.; Joshi, P.; Tadigadapa, S.; Eklund, Raman Scattering from High-Frequency Phonons in Supported n-Graphene Layer Films. *Nano Letters* **2006**, 6 (12), 2667-2673.
2. Scarpa, F.; Adhikari, S.; Gil, A.; Remillat, C. The bending of single layer graphene sheets: the lattice versus continuum approach. *Nanotechnology* **2010**, 21 (12), 125702.
3. Jiang, L. Y.; Huang, Y.; Jiang, H.; Ravichandran, G.; Gao, H.; Hwang, K.; Liu, B. A cohesive law for carbon nanotube/polymer interfaces based on the van der Waals force. *Journal of the Mechanics and Physics of Solids* **2006**, 54 (11), 2436-2452.
4. Girifalco, L. A.; M. Hodak, R. S. L. Carbon Nanotubes, Buckyballs, Ropes, and a Universal Graphitic Potential. *Phys. Rev. B* **2000**, 62, 13104–13110.
5. Kumar S.; Parks D.; Kamrin K. Mechanicistic Origin of the Ultrastrong Adhesion between Graphene and a-SiO₂: Beyond van der Waals. *ACS Nano* **2016**, 10 (7) 6552-6562.
6. Sadewasser, S.; Barth, C. Electrostatic Force Microscopy And Kelvin Probe Force Microscopy. In *Characterization of Materials*; John Wiley & Sons, Inc., 2002.

7. Long, F.; Yasaei, P.; Sanoj, R.; Yao, W.; Král, P.; Salehi-Khojin, A.; Shahbazian-Yassar, R. Characteristic Work Function Variations of Graphene Line Defects. *ACS Applied Materials & Interfaces* **2016**, 8 (28), 18360-18366.